Research Square

Preprints are preliminary reports that have not undergone peer review.
They should not be considered conclusive, used to inform clinical practice,
or referenced by the media as validated information.

Giant nonreciprocal resistance from mesoscopic phase coexistence

Fumitaka Kagawa

kagawa@phys.sci.isct.ac.jp

Institute of Science Tokyo https://orcid.org/0000-0002-1763-6799

Samiran Banu

RIKEN CEMS

Testuya Nomoto

RIKEN CEMS

kentaro Ino

Institute of Science Tokyo

Shogo Maeyama

Institute of Science Tokyo

Keisuke Matsuura

Institute of Science Tokyo

Article

Keywords:

Posted Date: April 19th, 2026

DOI: https://doi.org/10.21203/rs.3.rs-9379665/v1

License: This work is licensed under a Creative Commons Attribution 4.0 International License. Read Full License

Additional Declarations: There is **NO** Competing Interest.

Giant nonreciprocal resistance from mesoscopic phase coexistence

Samiran Banu[1], Tetsuya Nomoto[1], Kentaro Ino[2], Shogo Maeyama[2], Keisuke Matsuura[2], Fumitaka Kagawa[1, 2]*

[1] *RIKEN Center for Emergent Matter Science (CEMS), Wako 351-0198, Japan*

[2] *Department of Physics, Institute of Science Tokyo, Meguro 152-8551, Japan*

* Corresponding author: Fumitaka Kagawa (fumitaka.kagawa@riken.jp)

Abstract

Nonreciprocal electrical transport typically relies on inversion-symmetry breaking arising from noncentrosymmetric crystal structures or engineered structural asymmetry. Here we show that mesoscopic phase coexistence near a first-order transition induces inversion-symmetry breaking at intermediate length scales, thereby generating large nonreciprocal resistance. In the organic conductor α-(BEDT-TTF)$_2$I$_3$, a pronounced nonreciprocal resistance emerges exclusively in the phase-coexistence regime and vanishes in homogeneous phases, as revealed by transport measurements and spatially resolved Raman spectroscopy. The magnitude of the nonreciprocal resistance coefficient exceeds previously reported values in systems based on crystal noncentrosymmetry or engineered asymmetry by more than an order of magnitude. Importantly, the response can be controlled in a reversible and non-volatile manner using voltage pulses, indicating that electrically driven reconfiguration of domain textures modulates the nonreciprocal response. These results establish mesoscopic phase coexistence as a platform for generating and tuning nonreciprocal resistance and suggest a general design principle for inversion-symmetry-breaking nonlinear transport phenomena beyond nonreciprocal resistance.

Main

Nonreciprocal electrical transport[1–3], in which the resistance depends on the direction of current flow, has attracted considerable interest as a basis for diode-like functionalities in electronic systems. Such behaviour generally requires inversion-symmetry breaking and, in many cases, the breaking of time-reversal symmetry by an external magnetic field, and has been realized predominantly in materials with noncentrosymmetric crystal structures[1, 2, 4–15], as well as in engineered systems where structural asymmetry is introduced at the device level[16–20]. In particular, a commonly studied form is the *B*-linear nonreciprocal resistance[1–3], in which the electrical resistance acquires a component that is even in current and linear in an applied magnetic field *B*, leading to different resistances for opposite current directions (Fig. 1a, b). Nonreciprocal transport belongs to a broader class of nonlinear transport phenomena, including the nonlinear Hall effect[21–23], the superconducting diode effect[24–26], and the recently discovered nonlinear thermoelectric effect[27, 28]. To date, inversion-symmetry-breaking nonlinear transport phenomena have largely relied on intrinsic crystallographic

asymmetry or artificially designed structures, and are therefore typically tied to specific material symmetries or device geometries.

An alternative possibility is that inversion-symmetry breaking can emerge from spatial organization at intermediate, mesoscopic length scales, beyond crystal structure or device geometry. In many materials undergoing first-order phase transitions, electronic phase coexistence produces complex domain textures without characteristic periodicity, thereby introducing spatial asymmetry at mesoscopic scales (Fig. 1c). However, it remains unclear whether such mesoscopic phase coexistence can be harnessed as a practical design principle for generating and controlling inversion-symmetry breaking in transport. Here, we investigate this possibility using *B*-linear nonreciprocal resistance as a probe of inversion-symmetry breaking arising from mesoscopic phase coexistence.

Material properties

To this end, we focus on the organic conductor α-(BEDT-TTF)$_2$I$_3$ [BEDT-TTF: bis(ethylenedithio)-tetrathiafulvalene], which exhibits coexisting metallic and insulating regions near its first-order transition temperature. This material provides a natural platform in which strong resistivity contrast between coexisting domains and mesoscopic domain organization can be exploited to generate and enhance nonreciprocal responses. α-(BEDT-TTF)$_2$I$_3$ is a quasi-two-dimensional organic conductor consisting of alternating BEDT-TTF$^{+0.5}$ conducting layers and I_3^- insulating layers (Fig. 2a)[29, 30]. At high temperatures, the crystal is centrosymmetric (space group $P\bar{1}$). Upon cooling, the system undergoes a first-order transition to a charge-ordered (CO) insulating phase at $T_{CO} \approx 135$–136 K (ref. 29–33), below which the crystal symmetry becomes noncentrosymmetric ($P1$)[34–36]. This transition produces a resistivity change exceeding one order of magnitude within a narrow temperature interval, ≈ 2 K (Fig. 2b). Previous studies have shown that, near T_{CO}, high-temperature (high-*T*) metallic regions and low-temperature (low-*T*) insulating regions coexist and form mesoscopic multidomain patterns without any regular periodicity, with characteristic domain sizes reaching ~10 μm or larger[37]. These domain sizes are comparable to typical voltage-probe spacings (~0.1–1 mm), indicating that the spatial inhomogeneity persists over the measurement scale and may therefore give rise to nonreciprocal electrical responses.

To characterize the phase coexistence and determine its temperature range, we performed scanning Raman microscopy. From the Raman spectrum obtained at each spatial pixel, we extracted a local parameter ϕ_I that quantifies the relative spectral weight of the CO insulating phase and used it to reconstruct the domain distribution (for details of the procedure used to obtain domain images from the local Raman spectra, see the Methods section and Extended Data Fig. 1). The resulting temperature evolution of the domain structure is shown in Fig. 2c. Metallic and insulating regions form irregular domain patterns with a characteristic length scale of ~10 μm, consistent with previous reports[37]. Similar domain configurations are reproducibly recovered upon repeated cooling (Extended Data Fig. 2). Domains of the CO insulating phase begin to appear below ~140 K and grow progressively upon cooling until the transition is completed at ~128 K. From these images, we extracted the temperature dependence of the area fraction of the insulating phase, as shown in Fig. 2d. These results identify the temperature range of phase coexistence as 128–140 K. At lower

temperatures, phase coexistence disappears, and the system enters the fully charge-ordered insulating phase. In this phase, the crystal becomes intrinsically noncentrosymmetric ($P1$), rendering nonreciprocal electrical responses symmetry-allowed. This enables a direct comparison of the nonreciprocal response measured in the phase-coexistence regime and in the fully charge-ordered low-T phase, allowing us to assess the role of mesoscopic phase coexistence.

Observation of nonreciprocal resistance

To examine whether nonreciprocal resistance emerges in the phase-coexistence regime, we prepared a six-terminal device with electrodes 1–6 (Sample 1; lateral dimensions 620 μm × 1280 μm and thickness 82 μm), as shown in Fig. 2e. Electrodes 1 and 6 covered the sides of the sample using conducting carbon paste and were used to supply an approximately uniform electric current through the sample cross section, while electrodes 2–5 were used to probe the measurement-area dependence of the nonreciprocal voltage signal. Nonreciprocal resistance can be conveniently characterized by measuring the second-harmonic response of the voltage, $V^{2\omega}$, under the application of an alternating current $I(t) = I_0 \sin \omega t$ (ref. 14). Hereafter, $V^{2\omega}_{(m,n)}$ denotes the second-harmonic voltage measured between voltage electrodes m and n (m, n = 2–5).

Figure 2f shows the temperature dependence of the nonreciprocal resistance, defined as $R^{2\omega}_{(3,4)} \equiv V^{2\omega}_{(3,4)}/I_0$, under $I_0 = 45$ μA (corresponding to the current density $j_0 \approx 8.9 \times 10^2$ A m^{-2}) and a magnetic field B of ±5 T applied parallel to the current direction. A finite $R^{2\omega}$, approximately antisymmetric with respect to magnetic-field reversal, is observed exclusively in the temperature range between 125 and 139 K, coinciding with the regime of phase coexistence independently identified by scanning Raman microscopy (Fig. 2c and 2d). The observed $V^{2\omega}$ scales quadratically with I_0 (Extended Data Fig. 3). The signal shows at most a weak frequency dependence over 30–1000 Hz, with no sign of the strong attenuation expected for a thermally driven response (Extended Data Fig. 4), even though the typical roll-off frequency of thermal relaxation is ~1 Hz in bulk crystals[38]. These observations rule out a thermally driven origin and support an intrinsic second-harmonic response. The isothermal magnetic-field dependence of $R^{2\omega}_{(3,4)}$ is nearly linear in B with a negligible zero-field offset (Fig. 2g). The nonreciprocal signal remains finite in the $I \perp B$ configuration but is typically about one order of magnitude smaller than that in the $I \parallel B$ configuration (Extended Data Fig. 5). In the following, we therefore focus on the $I \parallel B$ configuration, where the signal allows more reliable quantitative analysis.

To quantify the magnitude of the B-linear and j-quadratic nonreciprocal voltage in a manner that facilitates comparison across different materials, the phenomenological coefficient $\hat{\gamma}$ [m^2 T^{-1} A^{-1}] is widely employed[10]. It is defined through $E(j) = \rho_0 j(1 + \hat{\gamma} B j + \cdots)$, or equivalently through $\rho^{2\omega}_{\mathrm{odd}}(B, j) = \frac{1}{2}\hat{\gamma}\rho^{1\omega} B j$, where $\rho^{2\omega}_{\mathrm{odd}}(B, j) \equiv [\rho^{2\omega}(B, j) - \rho^{2\omega}(-B, j)]/2$ and $\rho^{1\omega} = \rho_0$. In the present sample, $\hat{\gamma}_{(3,4)}$, derived from $R^{2\omega}_{(3,4)}$, exhibits a sharp peak around T_{CO}, reaching a maximum magnitude of 2.2×10^{-6} m^2 T^{-1} A^{-1} (Fig. 2h). Upon cooling, $\hat{\gamma}$ decreases rapidly within the phase-coexistence regime (for instance, $|\hat{\gamma}| \approx 7.0 \times 10^{-8}$ m^2 T^{-1} A^{-1} at 135 K) and further drops to $|\hat{\gamma}| \approx 2.9 \times 10^{-9}$ m^2 T^{-1} A^{-1} upon entering the intrinsically noncentrosymmetric low-T phase with no metal/insulator phase coexistence (125 K). These results indicate

that the B-linear nonreciprocal resistance in this system is closely associated with phase coexistence and cannot be explained solely by bulk inversion-symmetry breaking.

Spatial dependence of the nonreciprocal response

Having established that a finite nonreciprocal resistance emerges only in the vicinity of the transition temperature, we next examine its spatial signature associated with mesoscopic inversion-symmetry breaking by comparing measurements across different voltage-terminal pairs. Figure 3a shows the temperature dependence of the nonreciprocal resistance $R^{2\omega}_{(m,n)}$ measured for all voltage-terminal pairs during cooling. Both the sign and magnitude of $R^{2\omega}_{(m,n)}$ vary strongly with electrode configuration, with some pairs exhibiting positive signals, others negative, and one pair ($R^{2\omega}_{(4,5)}$) exhibiting a nearly vanishing response. This pronounced electrode-pair dependence is reproducible across thermal cycles (Extended Data Fig. 6) and is also observed in another specimen (Sample 3; Extended Data Fig. 7). Moreover, the second-harmonic voltage obeys voltage additivity, $V^{2\omega}_{(m,n)} = V^{2\omega}_{(m,k)} + V^{2\omega}_{(k,n)}$, within experimental accuracy (Extended Data Fig. 8). These observations confirm that the spatial variations reflect an intrinsic property of the sample rather than spurious effects, such as contact-related artifacts. Together with the confinement of the nonreciprocal response to the phase-coexistence regime, they demonstrate that the nonreciprocal response originates from mesoscopic inversion-symmetry breaking associated with spatially heterogeneous domain texture.

We next examine how the nonreciprocal-resistance coefficient $\hat{\gamma}_{(m,n)}$ evolves with electrode spacing. Figure 3b summarizes the maximum values of the nonreciprocal coefficient $\hat{\gamma}_{(m,n)}$ for each electrode pair in two specimens (Samples 1 and 3), plotted as a function of electrode spacing. While both the sign and magnitude vary substantially among different pairs, the overall magnitude of $|\hat{\gamma}_{(m,n)}|$ tends to decrease with increasing electrode spacing (Fig. 3c), showing a similar trend in both samples. This length-scale dependence reflects a spatial averaging of sign-varying local contributions to $R^{2\omega}_{(m,n)}$, combined with the monotonic increase of $R^{1\omega}_{(m,n)}$ with probe length, leading to a progressive suppression of $\hat{\gamma}_{(m,n)} = 2R^{2\omega}_{(m,n)}/(R^{1\omega}_{(m,n)}Bj)$ for widely separated electrodes. This behaviour indicates that the magnitude of the nonreciprocal coefficient ($\hat{\gamma}$), although correlated with the degree of inversion-symmetry breaking, is not an intrinsic material parameter in the present measurements but instead reflects the effective symmetry at the measurement scale. At larger length scales, mesoscopic spatial inhomogeneities are progressively averaged out, leading to a reduction in the effective inversion-symmetry breaking. This illustrates how nonlinear transport coefficients can be influenced by the interplay between mesoscopic domain structure and the measurement scale. Direct spatial correlation between the transport signal and the real-space domain texture is not straightforward in the present case, because transport reflects spatial averaging over ~200 μm scales, whereas Raman imaging probes only ~25 μm fields of view. Nevertheless, the consistency between the phase-coexistence window, electrode-pair dependence and heterogeneous domain patterns supports a mesoscopic origin of the observed nonreciprocity.

Comparison with previously reported nonreciprocal responses

To place our findings in a broader materials context, Table 1 summarizes representative nonreciprocal-resistance coefficients $\hat{\gamma}$ reported in systems where inversion-symmetry breaking originates from intrinsic crystallographic structure or engineered device asymmetry. Across these material classes, reported values of $\hat{\gamma}$ have so far remained below $\sim 10^{-7}$ m^2 T^{-1} A^{-1}. For example, the largest coefficients reported for crystallographically noncentrosymmetric systems, such as $ZrTe_5$ (ref. 6) or WTe_2 (ref. 7), are $\hat{\gamma} \approx$ (3–4) $\times 10^{-7}$ m^2 T^{-1} A^{-1}.

A representative magnitude, defined as the average of $|\hat{\gamma}|$ over six nearest-neighbor electrode pairs with 170–240 μm spacing across Samples 1 and 3, is $\hat{\gamma} \approx 5.9 \times 10^{-6}$ m^2 T^{-1} A^{-1}. Among these pairs, the maximum observed $\hat{\gamma}$ reaches $\approx 1.9 \times 10^{-5}$ m^2 T^{-1} A^{-1}. In the present system, $\hat{\gamma}$ reflects inversion-symmetry breaking arising from mesoscopic phase coexistence on the measurement scale and is progressively suppressed at larger electrode separations. It therefore should not be regarded as a strictly intrinsic bulk material constant. Nevertheless, the magnitude achieved in the present work exceeds the empirical ceiling observed in noncentrosymmetric crystals and engineered systems with broken inversion symmetry by more than an order of magnitude. This enhancement highlights mesoscopic phase coexistence as an efficient route to achieving large nonreciprocal coefficients and suggests a design strategy for amplifying nonreciprocal transport responses through mesoscale phase organization.

Voltage-pulse control of nonreciprocal resistance

Given the large nonreciprocal response observed in the phase-coexistence regime, an important question is whether it can be actively controlled, as such control would provide a basis for designing nonreciprocal transport functionalities. Here we demonstrate that nonreciprocal resistance arising from phase coexistence can be reversibly controlled by voltage pulses through electrically driven reconfiguration of mesoscopic domain textures. Voltage- or current-induced control of resistance has been reported in a wide range of systems exhibiting metal–insulator transitions[39–45], although the microscopic mechanisms of the resistance switching remain diverse and, in some cases, controversial. Specifically, α-(BEDT-TTF)$_2$I$_3$ exhibits a low-T CO phase that belongs to the polar point group 1 and thus carries a finite ferroelectric polarization[35]. An external electric field can therefore couple to this polarization and modify the relative free-energy balance between the metallic and CO phases. This suggests that voltage pulses can bias the formation or rearrangement of metal/CO domains in a polarity-dependent manner.

To test this idea, we applied alternating +4.2 V (≈ 33 V cm^{-1}) and –4.2 V voltage pulses (1 s duration) at 137.5 K within the phase-coexistence regime, with a waiting time of 100 s between successive pulses. The pulse sequence is illustrated in Fig. 4a. $R^{1\omega}_{(3,4)}$ and $R^{2\omega}_{(3,4)}$ were tracked as a function of time. Figure 4b shows the evolution of the linear resistance $R^{1\omega}_{(3,4)}$ before and after each pulse. The change is polarity-dependent but small (~1%, $\Delta R^{1\omega}_{(3,4)} \approx 1.5$ Ω), comparable to the level of fluctuations (~1 Ω) in the measured data, which would correspond to temperature variations of ~4 mK. In contrast, the nonreciprocal component $R^{2\omega}_{(3,4)}$ (Fig. 4c) shows a more pronounced polarity-dependent modulation. By changing the pulse magnitude intermittently from +4.5 V to –4.5 V and back to +4.5 V, a clear hysteresis loop with a magnitude change of approximately 14% is observed (Fig. 4d), indicating reversible control of the nonreciprocal response. These

results establish electrically driven domain reconfiguration as an effective mechanism for tuning nonreciprocal transport and provide a route toward functional control of nonlinear electronic responses in phase-coexisting materials.

Discussion and outlook

The present results demonstrate that nonreciprocal electrical transport can be governed by inversion-symmetry breaking emerging at mesoscopic length scales, with the effective degree of symmetry breaking determined by the measurement scale. This route to inversion-symmetry breaking is qualitatively distinct from those based on crystal noncentrosymmetry or engineered device asymmetry. The microscopic processes underlying nonreciprocal transport with pronounced magnitudes in α-(BEDT-TTF)$_2$I$_3$ remain an open question and likely depend on material-specific details. In multidomain configurations with broken inversion symmetry, possible contributions include inhomogeneous current distribution, transport across domain walls, or scattering processes. These considerations nevertheless suggest that similar effects can arise in a broad class of materials undergoing first-order transitions accompanied by mesoscopic phase coexistence. For example, in the kagome metal CsV_3Sb_5, a pronounced $V^{2\omega}$ signal has been reported near the charge-density-wave (CDW) transition[46], where a narrow phase-coexistence regime has been identified[47]. Because the inversion-symmetry breaking identified here arises from mesoscopic domain configurations rather than crystal noncentrosymmetry or engineered structural asymmetry, this mechanism may be applicable to a wide range of materials exhibiting first-order transitions and could also extend to other inversion-symmetry-breaking nonlinear transport phenomena.

Acknowledgements

F.K. thanks T.-h.Arima and H. Ishizuka for fruitful discussions. This research was supported by the Japan Society for the Promotion of Science (KAKENHI Grant Nos. 18J20362 to T.N., and 25K00944 and JP26H00383 to F.K.).

Author contributions

F.K. conceived and supervised the project. T.N. performed the sample synthesis. S.B. conducted the transport measurements. K.I., S.M., and K.M. performed the scanning Raman microscopy. S.B. and F.K. analysed the transport data. K.I. and K.M. analysed the scanning Raman data. F.K. wrote the original draft. All authors commented on the manuscript.

Corresponding author

Correspondence and requests for materials should be addressed to Fumitaka Kagawa.

Competing interests

The authors declare that they have no competing interests.

Data Availability

All data are available from the corresponding author upon request. Source data are provided with the paper.

References

1. Krstić, V., Roth, S., Burghard, M., Kern, K. & Rikken, G. L. J. A. Magneto-chiral anisotropy in charge transport through single-walled carbon nanotubes. *J. Chem. Phys.* **117**, 11315–11319 (2002).
2. Pop, F., P. A.-Senzier, Canadell, E., Rikken, G. L. J. A. & Avarvari, N. Electrical magnetochiral anisotropy in a bulk chiral molecular conductor. *Nat. Commun.* **5**, 3757 (2014).
3. Tokura, Y. & Nagaosa, N. Nonreciprocal responses from non-centrosymmetric quantum materials. *Nat. Commun.* **9**, 3740 (2018).
4. Rikken, G. L. J. A. & Avarvari, N. Strong electrical magnetochiral anisotropy in tellurium. *Phys. Rev. B* **99**, 245153 (2019).
5. Ideue, T. et al. Bulk rectification effect in a polar semiconductor. *Nat. Phys.* **13**, 578–583 (2017).
6. Wang, Y. et al. Gigantic magnetochiral anisotropy in the topological semimetal $ZrTe_5$. *Phys. Rev. Lett.* **128**, 176602 (2022).
7. Yokouchi, T., Ikeda, Y., Morimoto, T. & Shiomi, Y. Giant magnetochiral anisotropy in Weyl semimetal WTe_2 induced by diverging Berry curvature. *Phys. Rev. Lett.* **130**, 136301 (2023).
8. Wang, R. et al. Nonvolatile electrical switching of nonreciprocal transport in ferroelectric polar metal WTe_2. *Nat. Commun*. **16**, 11298 (2025).
9. Yokouchi, T. et al. Electrical magnetochiral effect induced by chiral spin fluctuations. *Nat. Commun*. **8**, 866 (2017).
10. Aoki, R., Kousaka, Y. & Togawa, Y. Anomalous nonreciprocal electrical transport on chiral magnetic order. *Phys. Rev. Lett.* **122**, 057206 (2019).
11. Masuda, H. et al. Room temperature chirality switching and detection in a helimagnetic $MnAu_2$ thin film. *Nat. Commun*. **15**, 1999 (2024).
12. Wakatsuki, R. et al. Nonreciprocal charge transport in noncentrosymmetric superconductors. *Sci. Adv.* **3**, e1602390 (2018).
13. Zhang, E. et al. Nonreciprocal superconducting $NbSe_2$ antenna. *Nat. Commun.* **11**, 5634 (2020).
14. Ideue, T., Koshikawa, S., Namiki, H., Sasagawa, T. & Iwasa, Y. Giant nonreciprocal magnetotransport in bulk trigonal superconductor $PbTaSe_2$. *Phys. Rev. Research* **2**, 042046(R) (2020).
15. Zhang, Y. et al. Nonreciprocal charge transport in superconductor $ZrTe_3$. *Phys. Rev. B* **112**, 115440 (2025).
16. Rikken, G. L. J. A. & Wyder, P. Magnetoelectric anisotropy in diffusive transport. *Phys. Rev. Lett*. **94**, 016601 (2005).
17. Yasuda, K. et al. Large unidirectional magnetoresistance in a magnetic topological insulator. *Phys. Rev. Lett.* **117**, 127202 (2016).

18. Choe, D. et al. Gate-tunable giant nonreciprocal charge transport in noncentrosymmetric oxide interfaces. *Nat. Commun*. **10**, 4510 (2019).
19. Rikken, G. L. J. A., Fölling, J. & Wyder, P. Electrical magnetochiral anisotropy. *Phys. Rev. Lett.* **87**, 236602 (2001).
20. Birch, M. T. et al. Nanosculpted 3D helices of a magnetic Weyl semimetal with switchable nonreciprocal electron transport. *Nat. Nanotechnol.* 10.1038/s41565-025-02104-x075141 (2026).
21. Ma, Q. et al. Observation of the nonlinear Hall effect under time-reversal-symmetric conditions. *Nature* **565**, 337–342 (2019).
22. Du, Z. Z., Lu, H. Z. & Xie, X. C. Nonlinear Hall effects. *Nat. Rev. Phys*. **3**, 744–752 (2021).
23. Gao, A. et al. Quantum metric nonlinear Hall effect in a topological antiferromagnetic heterostructure. *Science* **381**, 181–186 (2023).
24. Ando, F., Miyasaka, Y., Li, T., Ishizuka, J., Arakawa, T., Shiota, Y., Moriyama, T., Yanase, Y. & Ono, T. Observation of superconducting diode effect. *Nature* **584**, 373–376 (2020).
25. Baumgartner, C. et al. Supercurrent rectification and magnetochiral effects in symmetric Josephson junctions. *Nat. Nanotechnol.* **17**, 39–44 (2022).
26. Nadeem, M., Fuhrer, M. D. & Wang, X. The superconducting diode effect. *Nat. Rev. Phys*. **5**, 558–577 (2023).
27. Liu, H. et al. Nonlinear Nernst effect in trilayer graphene at zero magnetic field. *Nat. Nanotechnol.* **20**, 1221–1227 (2025).
28. Nomoto, T., Kikkawa, A., Nakazawa, K., Yamaguchi, T. & Kagawa, F. Observation of the nonlinear chiral thermoelectric Hall effect in tellurium. *Nat. Phys.* **21**, 1920–1925 (2025).
29. Bender, K. et al. Synthesis, structure and physical properties of a two-dimensional organic metal, di[bis(ethylenedithiolo)tetrathiofulvalene] triiodide, (BEDT-TTF)$_2$I$_3$. *Mol. Cryst. Liq. Cryst.* **108**, 359–371 (1984).
30. Ivek, T. et al. Semimetallic and charge-ordered α-(BEDT-TTF)$_2$I$_3$: On the role of disorder in dc transport and dielectric properties. *Phys. Rev. B* **96**, 075141 (2017).
31. Fortune, N. A. et al. Calorimetric observation of the metal-insulator phase transition in α-(BEDT-TTF)$_2$I$_3$. *Solid State Commun.* **79**, 265–269 (1991).
32. Yakushi, K. et al. Temperature dependence of the reflectance spectra of the single crystals of bis(ethylenedithio)tetrathiafulvalene salts. *Bull. Chem. Soc. Jpn*. **60**, 4251–4257 (1987).
33. Takano, Y. et al. Charge disproportionation in the organic conductor α-(BEDT-TTF)$_2$I$_3$. *J. Phys. Chem. Solids* **62**, 393–395 (2001).
34. Kakiuchi, T. et al. Charge ordering in α-(BEDT-TTF)$_2$I$_3$ by synchrotron X-ray diffraction. *J. Phys. Soc. Jpn.* **76**, 113702 (2007).
35. Yamamoto, K. et al. Strong optical nonlinearity and its ultrafast response associated with electron ferroelectricity in an organic conductor. *J. Phys. Soc. Jpn*. **77**, 074709 (2008).
36. Kiswandhi, A. & Osada, T. Observation of possible nonlinear anomalous Hall effect in organic two-dimensional Dirac fermion system. *J. Phys.: Condens. Matter* **34**, 105602 (2022).

37. Pustogow, A. et al. Internal strain tunes electronic correlations on the nanoscale. *Sci. Adv*. **4**, eaau9123 (2018).
38. Furuta, S. et al. Reconsidering nonlinear emergent inductance: Time-varying Joule heating and its impact on AC electrical response. *Phys. Rev. B* **110**, 174402 (2024).
39. Zimmers, A. et al. Role of thermal heating on the voltage induced insulator-metal transition in VO_2. *Phys. Rev. Lett*. **110**, 056601 (2013).
40. Shukla, N. et al. Electrically induced insulator-to-metal transition in epitaxial $SmNiO_3$ thin films. *Appl. Phys. Lett*. **105**, 012108 (2014).
41. del Valle, J. et al. Dynamics of the electrically induced insulator-to-metal transition in rare-earth nickelates. *Phys. Rev. B* **104**, 165141 (2021).
42. Salev, P. et al. Transverse barrier formation by electrical triggering of a metal-to-insulator transition. *Nat. Commun*. **12**, 5499 (2021).
43. Adda, C. et al. Direct observation of the electrically triggered insulator-metal transition in V_3O_5 far below the transition temperature. *Phys. Rev. X* **12**, 011025 (2022).
44. Valmianski, I. et al. Origin of the current-driven breakdown in vanadium oxides: Thermal versus electronic. *Phys. Rev. B* **98**, 195144 (2018).
45. Kalcheim, Y. et al. Non-thermal resistive switching in Mott insulator nanowires. *Nat. Commun*. **11**, 2985 (2020).
46. Guo, C. et al. Switchable chiral transport in charge-ordered kagome metal CsV_3Sb_5. *Nature* **611**, 461–466 (2022).
47. Song, D. W. et al. Orbital ordering and fluctuations in a kagome superconductor CsV_3Sb_5. *Sci. China Phys. Mech. Astron*. **65**, 247462 (2022).

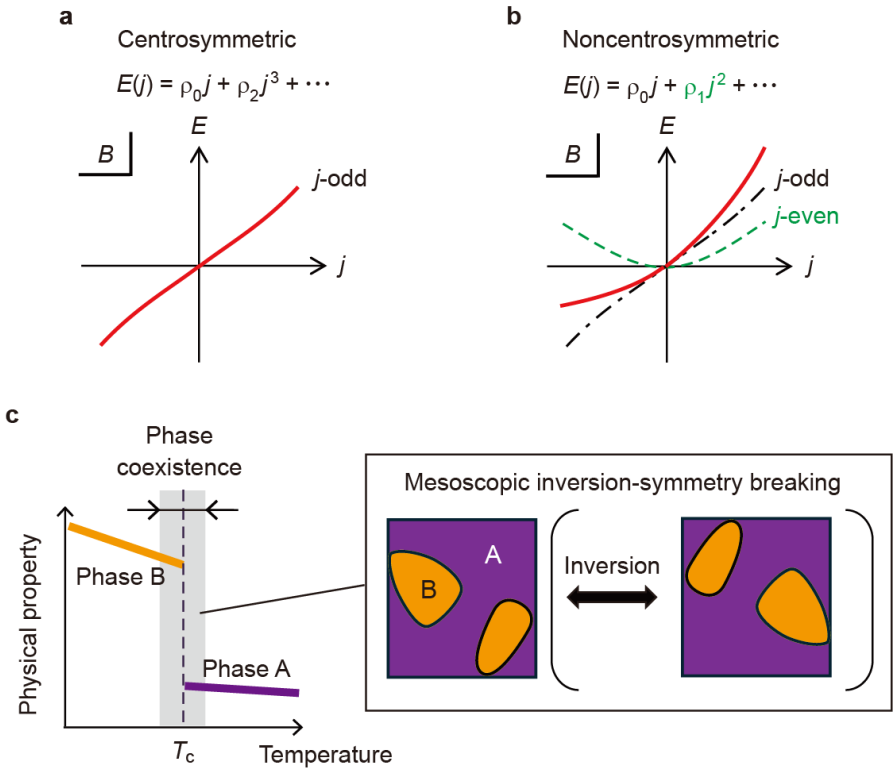

Fig. 1 | Inversion-symmetry breaking from mesoscopic phase coexistence. a, b, Expected current–voltage characteristics in a magnetic field for centrosymmetric (**a**) and noncentrosymmetric (**b**) systems. In centrosymmetric systems, the current–voltage relation is an odd function of current, whereas in inversion-symmetry-broken systems an even-in-current term, $\rho_1 j^2$, is allowed, resulting in nonreciprocal resistance in a magnetic field. **c,** Schematic illustration of inversion-symmetry breaking arising from mesoscopic phase coexistence near a first-order phase transition.

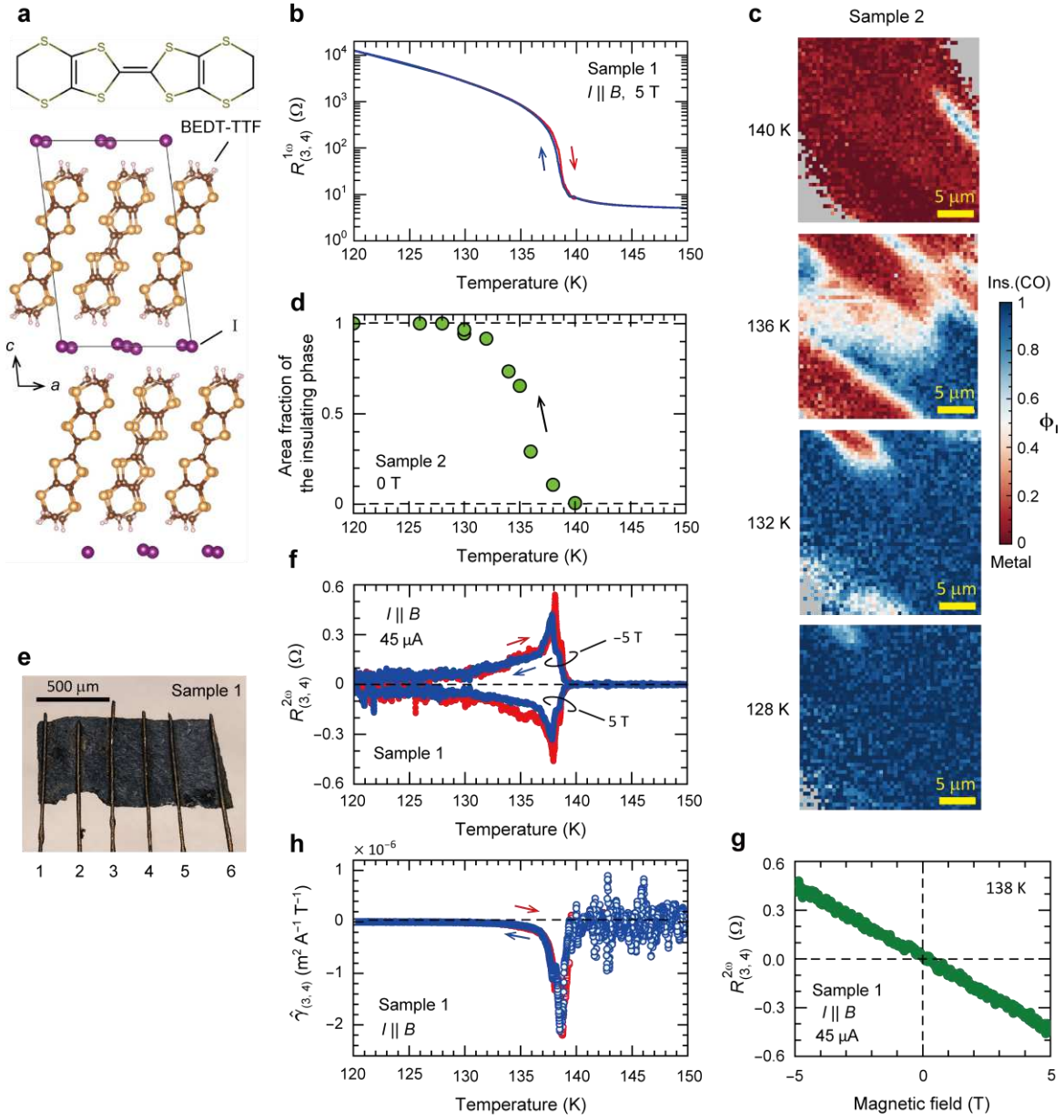

Fig. 2 | Emergence of nonreciprocal resistance in the phase-coexisting regime of α-(BEDT-TTF)$_2$I$_3$. a, Crystal structure of α-(BEDT–TTF)$_2$I$_3$, consisting of alternating conducting BEDT–TTF cation layers and insulating I_3 anion layers. **b,** Temperature dependence of the resistivity, showing the metal–insulator transition. **c,** Temperature evolution of the real-space phase distribution obtained by scanning Raman microscopy. The colour scale represents the parameter ϕ_I, which quantifies the relative spectral weight of the charge-ordered (CO) insulating phase. Gray-shaded areas indicate regions where a reliable Raman signal was not obtained and were therefore excluded from the analysis. Scale bars are 5 μm. **d,** Temperature evolution of the area fraction of the CO insulating phase extracted from the Raman images. Pixels with $\phi_I \geq 0.65$ are classified as the insulating phase. **e,** Photograph of Sample 1 with six electrodes. **f,** Temperature dependence of $R^{2\omega}_{(3,4)}$ under magnetic fields of ±5 T. **g,** Magnetic field dependence of $R^{2\omega}_{(3,4)}$ at 138 K. **h,** Temperature dependence of the nonreciprocal-resistance coefficient, $\hat{\gamma}$. Transport measurements shown in panels **b** and **f**–**h** were performed on Sample 1 in the $I \parallel B$ configuration.

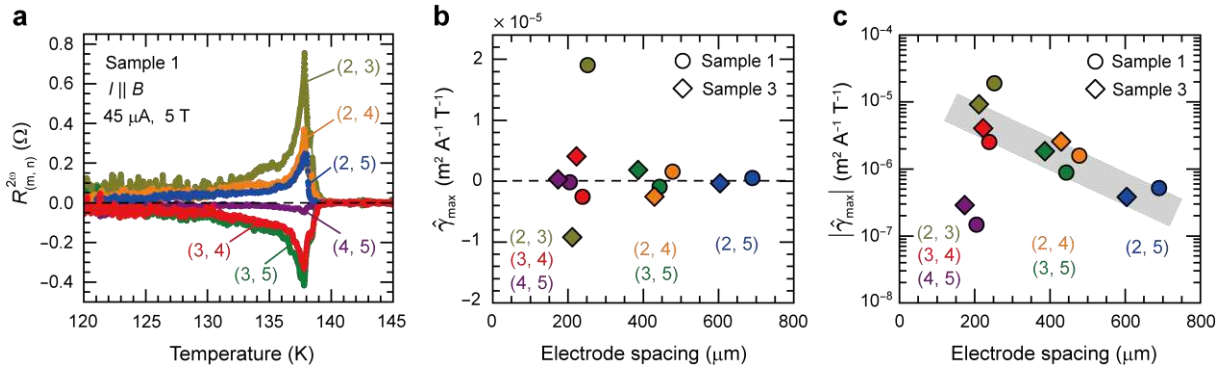

Fig. 3 | Spatial characteristics of the nonreciprocal resistance. a, Temperature dependence of the nonreciprocal resistance $R^{2\omega}_{(m,n)}$ measured for all voltage-terminal pairs during cooling (Sample 1). **b, c,** Maximum value of $\hat{\gamma}_{(m,n)}$ for each electrode pair in Samples 1 and 3 versus electrode spacing, plotted on linear (**b**) and logarithmic (**c**) scales. Panel **c** shows the absolute value $|\hat{\gamma}_{(m,n)}|$. Within the limited number of electrode configurations explored here, $|\hat{\gamma}_{(m,n)}|$ systematically decreases with increasing electrode spacing.

Table 1 | Representative values of the nonreciprocal-resistance coefficient $\hat{\gamma}$ reported in selected material systems, grouped by the origin of inversion-symmetry breaking. Only selected examples are shown for each category. The largest representative value reported here exceeds previously reported values by approximately an order of magnitude. The last row highlights the present work, which exhibits a mesoscopic route to inversion-symmetry breaking through spontaneously formed mesoscopic domain textures. For this work, the reported value corresponds to the magnitude averaged over six nearest-neighbor electrode pairs with electrode spacings of approximately 170–240 μm across two specimens (Samples 1 and 3), as the coefficient depends on the electrode configuration and the mesoscopic domain texture.

Materials	$\hat{\gamma}$ [$m^2\ T^{-1}\ A^{-1}$]	Origin of inversion-symmetry breaking	Ref.
$ZrTe_5$ (largest reported), WTe_2	$(3–4) \times 10^{-7}$	Crystal noncentrosymmetry	6, 7
$[DM\text{-}EDT\text{-}TTF]_2ClO_4$	1×10^{-10}	Crystal noncentrosymmetry	2
$PbTaSe_2$ flake (superconducting)	1×10^{-8}	Crystal noncentrosymmetry	14
$MnAu_2$ thin film	$(0.8–1) \times 10^{-13}$	Chiral magnetic order	11
Cr-doped $(Bi, Sb)_2Te_3$ / $(Bi, Sb)_2Te_3$	$(0.3–1.4) \times 10^{-9}$	Heterostructure stacking	17
Macroscopic Bi helices	3×10^{-10}	Geometric chirality	19
Nanosculpted $Co_3Sn_2S_2$ helices	$(0.7–4) \times 10^{-14}$	Geometric chirality	20
α-$(BEDT\text{-}TTF)_2I_3$	$\mathbf{5.9 \times 10^{-6}}$	**Mesoscopic phase coexistence**	**This work**

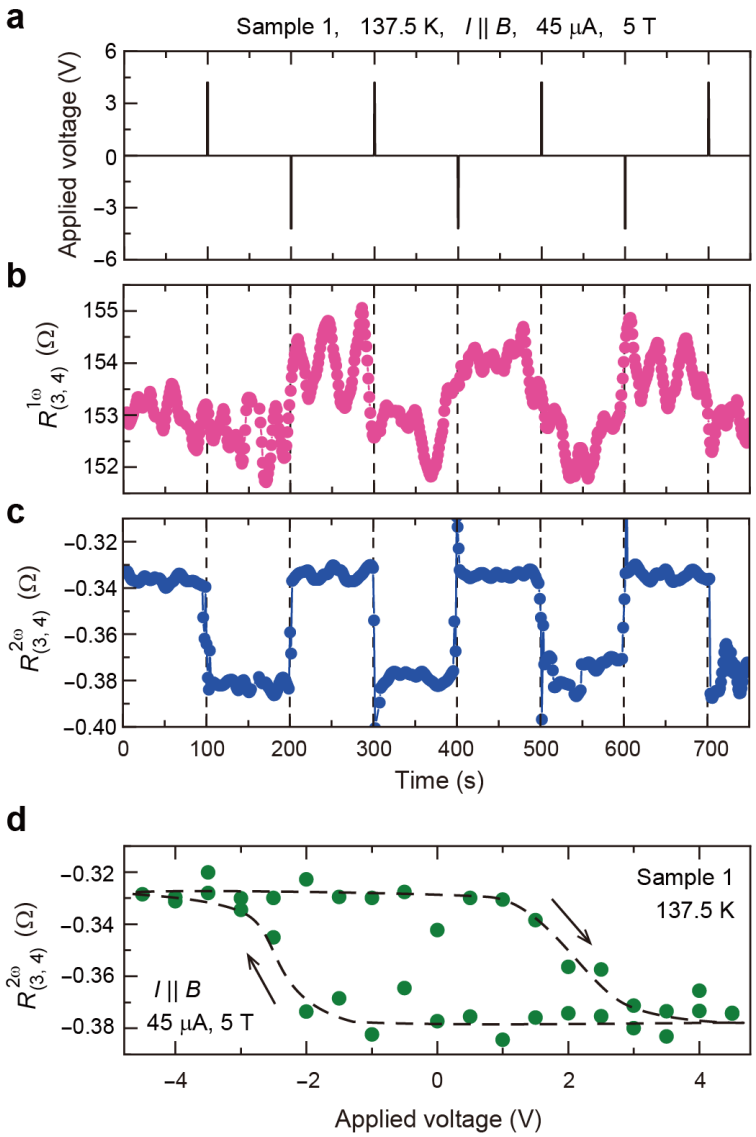

Fig. 4 | Electrical control of nonreciprocal resistance using voltage pulses in Sample 1. a, Voltage-pulse protocol used to control the metallic and charge-ordered (CO) domain texture in the phase-coexistence regime. Alternating ±4.2 V pulses (1 s duration) are applied at 137.5 K in a magnetic field of 5 T. **b, c,** Pulse-induced switching of the linear-response resistance $R^{1\omega}_{(3,4)}$ (**b**) and the nonreciprocal resistance $R^{2\omega}_{(3,4)}$ (**c**), revealing only a modest change in $R^{1\omega}_{(3,4)}$ (~1%), whereas $R^{2\omega}_{(3,4)}$ is modulated by ~14%. **d,** Hysteresis of the nonreciprocal resistance induced by voltage pulses.

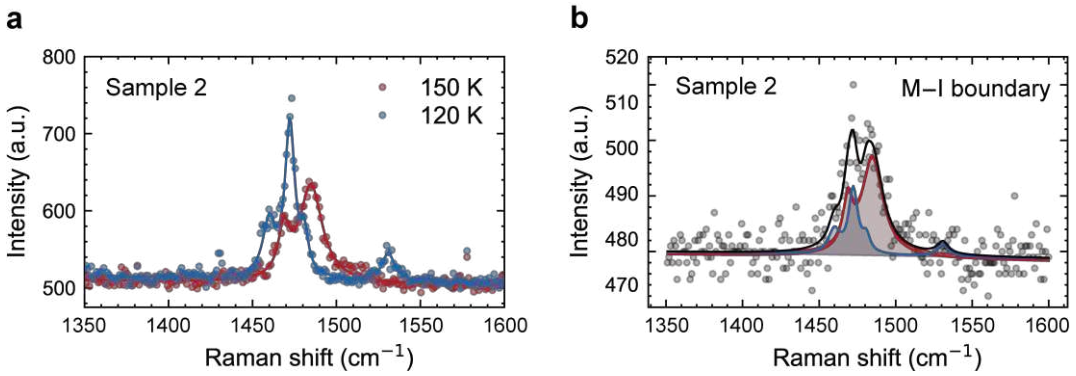

Extended Data Fig. 1 | Raman spectra obtained from individual pixels in the high-temperature metallic phase, the low-temperature insulating phase, and at a metal–insulator boundary. a, Typical Raman spectra obtained from single pixels in the high-temperature metallic (M) phase (150 K) and the low-temperature insulating (I) phase (120 K). These spectra were used as reference spectra to decompose the local Raman spectra measured in the phase-coexistence regime near the transition temperature. **b,** Example of the decomposition of a Raman spectrum obtained from a pixel located at a metal–insulator phase boundary in the phase-coexistence regime into contributions from the high-temperature and low-temperature phases.

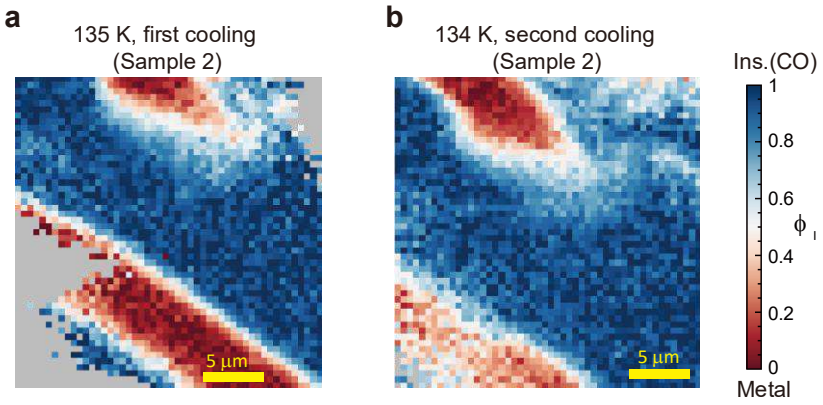

Extended Data Fig. 2 | Reproducibility of Raman-imaged domain structures across thermal cycles. Raman images acquired at 135 K during the first cooling (**a**) and at 134 K during the second cooling (**b**). Gray-shaded areas indicate regions where a reliable Raman signal was not obtained and were therefore excluded from the analysis. The scale bar is 5 µm.

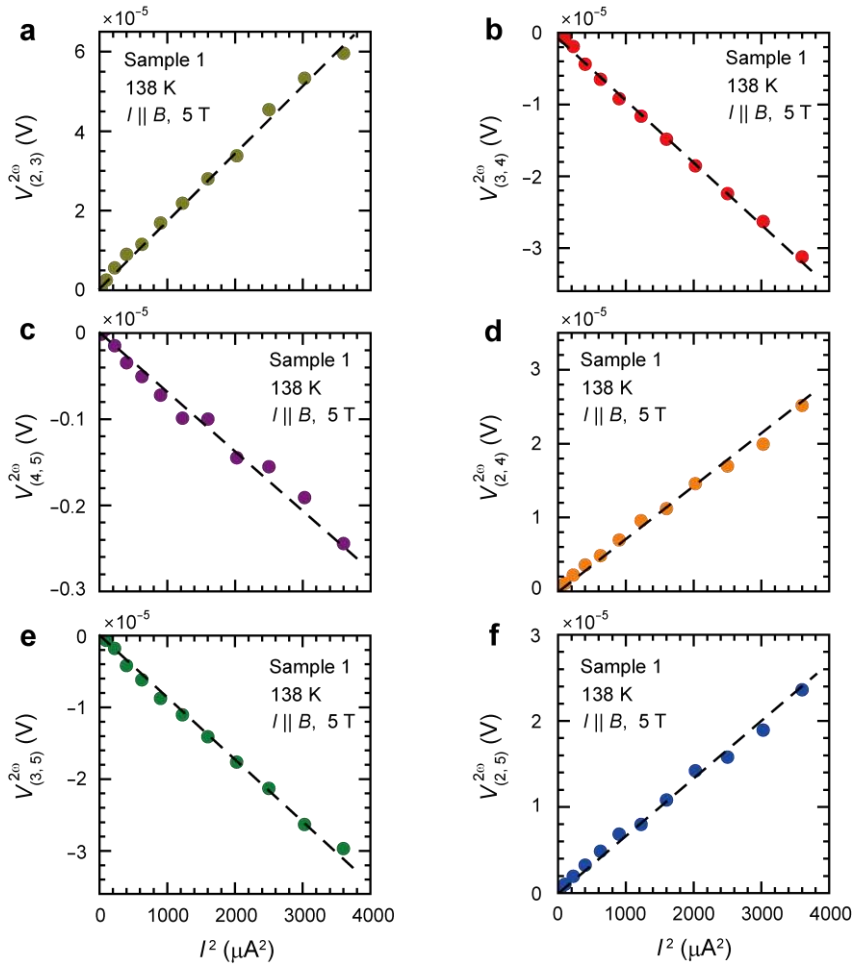

Extended Data Fig. 3 | Scaling of $V^{2\omega}_{(m,n)}$ with applied electric current for all electrode pairs in Sample 1. a–f, $V^{2\omega}_{(m,n)}$ plotted against the square of the AC current amplitude for all electrode pairs: **a,** $V^{2\omega}_{(2,3)}$, **b,** $V^{2\omega}_{(3,4)}$, **c,** $V^{2\omega}_{(4,5)}$ **d,** $V^{2\omega}_{(2,4)}$, **e,** $V^{2\omega}_{(3,5)}$, and **f,** $V^{2\omega}_{(2,5)}$. The measurements were performed at 5 T in the phase-coexistence regime (138 K). In the experiments shown in the main text, we used 45 μA.

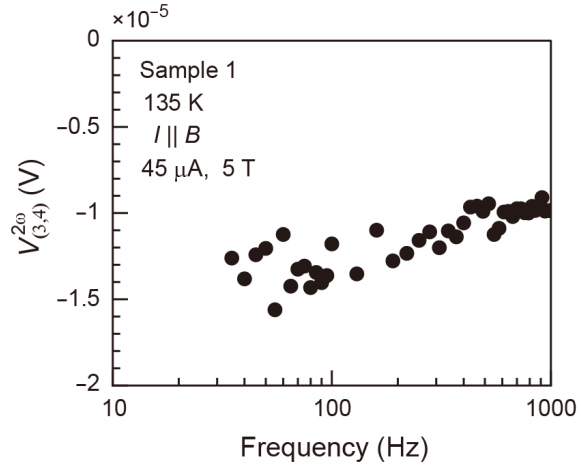

Extended Data Fig. 4 | Frequency dependence of $V_{(3,4)}^{2\omega}$ in Sample 1. The signal magnitude exhibits only weak dependence on frequency over the range 30–1000 Hz. In the experiments shown in the main text, we used 77.77 Hz.

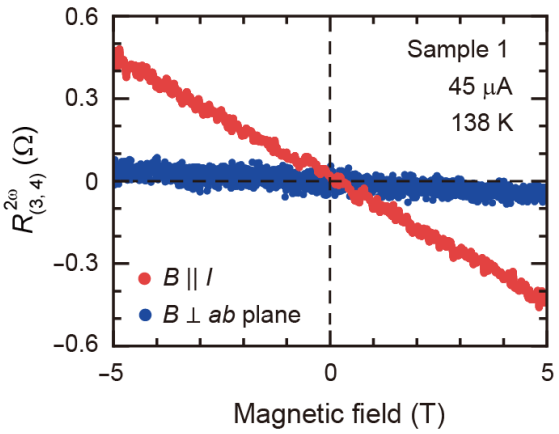

Extended Data Fig. 5 | Magnetic-field dependence of $R^{2\omega}_{(3,4)}$ for the $B \parallel I$ and $B \perp ab$-plane (conducting plane) configurations in the phase-coexistence regime (138 K) in Sample 1.

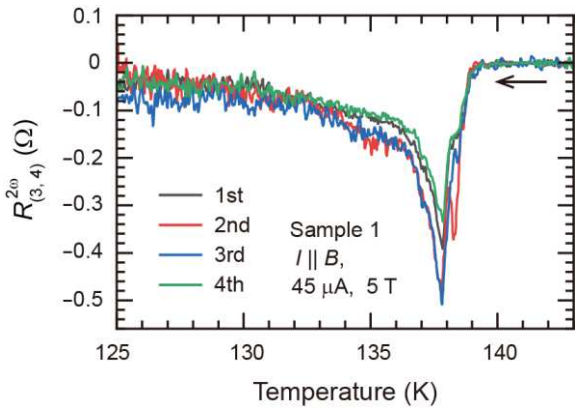

406

407

408 **Extended Data Fig. 6 | Comparison of the temperature dependence of $V^{2\omega}_{(3,4)}$ for different cooling runs**

409 **in Sample 1.**

410

411

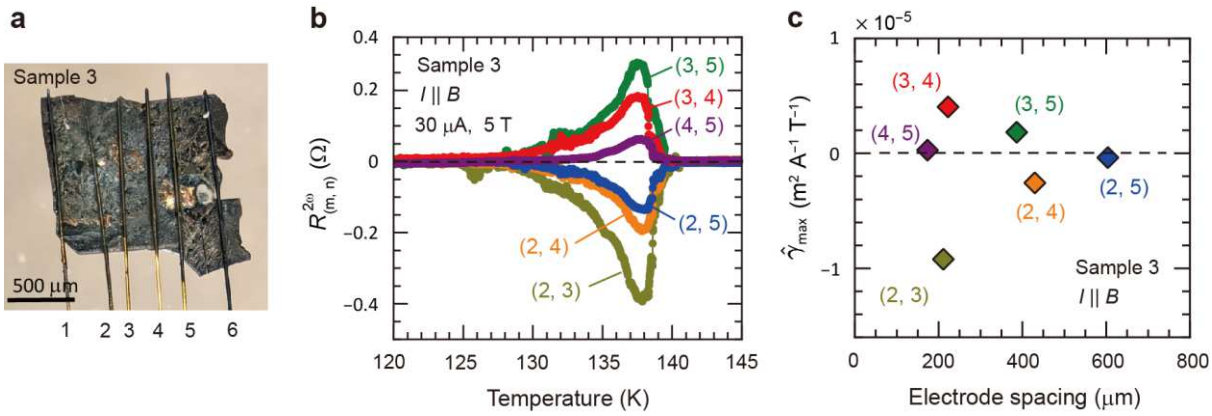

412

413

414 **Extended Data Fig. 7 | Spatial characteristics of the nonreciprocal resistance in Sample 3. a,** Photograph
415 of Sample 3 with six electrodes. **b,** Temperature dependence of the nonreciprocal resistance $R^{2\omega}_{(m,n)}$ measured
416 for all voltage-terminal pairs during cooling. **c,** Maximum values of $\hat{\gamma}_{(m,n)}$ for each electrode pair in Sample
417 3 versus electrode spacing.

418

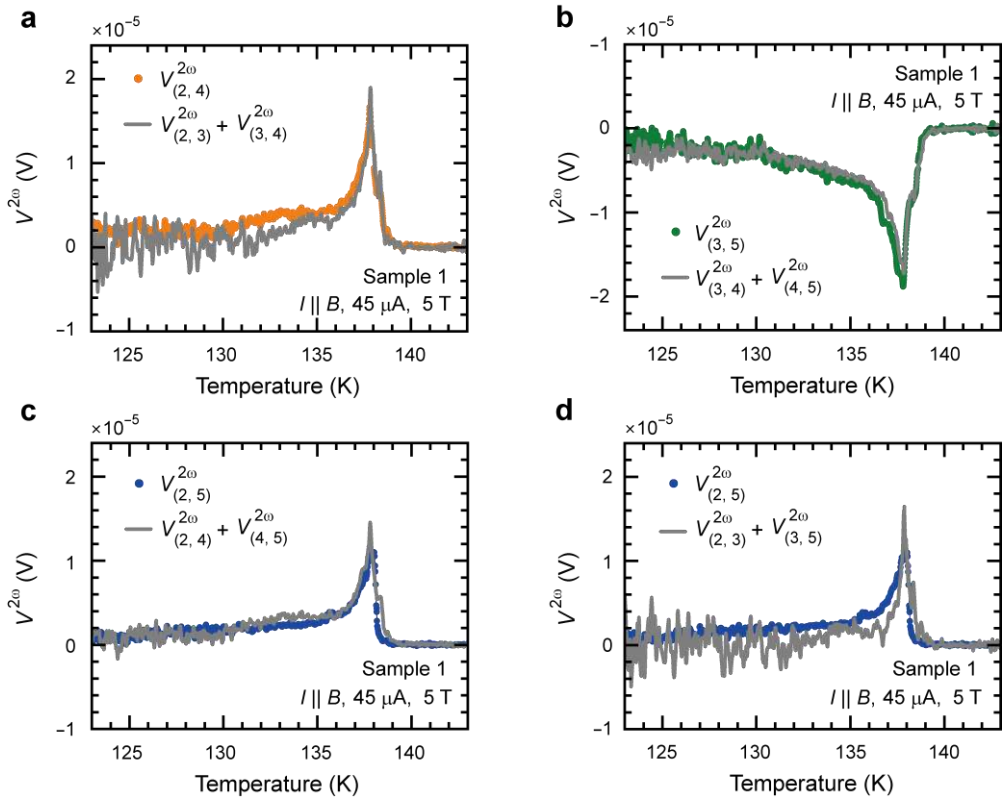

Extended Data Fig. 8 | Comparison of the temperature dependence of $V^{2\omega}_{(m,n)}$ with that of the sum $V^{2\omega}_{(m,k)} + V^{2\omega}_{(k,n)}$ in Sample 1 upon cooling. The temperature dependences for the individual electrode pairs were obtained during different cooling runs.

Method

Sample Preparation

Single crystals of α-(BEDT–TTF)$_2$I$_3$ were grown by electrochemical oxidation following established procedures for BEDT–TTF charge-transfer salts[29]. The electrochemical cell employed platinum electrodes and was operated at room temperature (20–25 °C) under an argon atmosphere to prevent solvent degradation. BEDT–TTF (7.6 mg) and tetra-*n*-butylammonium triiodide ($TBA^+I_3^-$; 76.6 mg, where $TBA^+ = (C_4H_9)_4N^+$) were dissolved in 15 mL of anhydrous tetrahydrofuran (THF) to prepare the electrolyte. Plate-like black crystals of α-(BEDT–TTF)$_2$I$_3$ gradually formed on the anode surface. The crystals were collected, rinsed with anhydrous THF, and dried under vacuum prior to characterization.

Transport measurements

The AC transport measurements were performed in a commercial cryostat equipped with a superconducting magnet. An AC current at a frequency of 77.77 Hz was applied using a current source (Keithley 6221), and the voltage outputs $V^{1\omega}$ and $V^{2\omega}$ were detected using two lock-in amplifiers (Stanford Research Systems, SR860 and SR865, respectively). Electrical contacts were fabricated by applying carbon paste to the crystal, forming six electrodes for transport measurements. To eliminate possible cross-talk between different voltage-terminal pairs, the voltage measurement was performed for only one (m, n) pair at a time. When acquiring temperature dependences for different electrode pairs, the lock-in connections were physically reconfigured for each measurement. For the pulsed-current measurements presented in Fig. 4, the analog output voltages $V^{1\omega}$ and $V^{2\omega}$ from the lock-in amplifiers were monitored with an oscilloscope (Tektronix, MDO3102).

Scanning Raman microscopy

Low-temperature Raman imaging was carried out using a commercial confocal Raman microscope (attoRAMAN, attocube). A low-temperature compatible objective (NA = 0.82; LT-APO 532-RAMAN, attocube) was positioned inside the cryostat approximately 500 μm above the sample surface, yielding a spatial resolution of ≈ 400 nm. The excitation source was a frequency-doubled Nd:YAG laser (λ = 532 nm). During imaging, the laser power was limited to 60 μW to minimize local heating. Scattered light was collected through a single-mode fiber and analysed using a spectrometer equipped with a 1,800 lines mm^{-1} grating. All measurements employed linearly polarized excitation. Raman maps were recorded over a 25 μm × 25.5 μm region with a step size of 500 nm × 500 nm.

For domain visualization using the scanning Raman microscopy, we first obtained Raman spectra $f(\omega)$ at 150 K and 120 K with a relatively long data-acquisition time (300 s) and analysed them using Lorentzian functions to obtain reference spectra of the high-temperature metallic (M) and low-temperature insulating (I) phases, $f_{\mathrm{M}}^{(\mathrm{ref})}(\omega)$ and $f_{\mathrm{I}}^{(\mathrm{ref})}(\omega)$ (Extended Data Fig. 1), respectively, as follows:

$$f(\omega) = a_0 + a_1\omega + \sum_i c_i \frac{\Gamma_i^2}{(\omega-\omega_i)^2+\Gamma_i^2} \equiv a_0 + a_1\omega + f_{\mathrm{M/I}}^{(\mathrm{ref})}(\omega),$$

where $a_0 + a_1\omega$ represents a linear-in-frequency background and c_i denotes the amplitude of the i-th Lorentzian peak. Local Raman spectra acquired at each spatial pixel with a data-acquisition time of 60 s were then fitted to a linear combination of $f_{\mathrm{M}}^{(\mathrm{ref})}(\omega)$ and $f_{\mathrm{I}}^{(\mathrm{ref})}(\omega)$:

$$f(\omega) = a_0 + a_1\omega + A\left[\phi_{\mathrm{I}} f_{\mathrm{I}}^{(\mathrm{ref})}(\omega) + (1-\phi_{\mathrm{I}}) f_{\mathrm{M}}^{(\mathrm{ref})}(\omega)\right],$$

where ϕ_{I} represents the relative spectral weight of $f_{\mathrm{I}}^{(\mathrm{ref})}(\omega)$ in the observed spectrum, and A is an intensity scaling factor that varies across the sample surface. The fitting coefficient ϕ_{I}, indicated by the colour bar, was used to generate Raman images. In Fig. 2d, pixels with $\phi_{\mathrm{I}} \geq 0.65$ are classified as the insulating phase. An example of the spectral decomposition is shown in Extended Data Fig. 1, and the temperature evolution of the domain texture is shown in Fig. 2c. For pixels with $A < 0.05$, the spectrum was considered unreliable due to insufficient signal intensity and was therefore excluded from the analysis; such pixels are indicated in gray in the Raman images.